Biogeochemistry (2023) 166:87–107
https://doi.org/10.1007/s10533-023-01094-z

Influence of contrasting redox conditions on iron (oxyhydr) oxide transformation and associated phosphate sorption

Maximilian Barczok · Chelsea Smith · Nicolle Di Domenico · Lauren Kinsman-Costello · David Singer · Elizabeth Herndon

Received: 29 June 2023 / Accepted: 16 October 2023 / Published online: 18 November 2023

Abstract Iron (oxyhydr)oxides strongly adsorb phosphate and limit its bioavailability, but interactions between phosphate and various Fe (oxyhydr)oxides are poorly constrained in natural systems. An in-situ incubation experiment was conducted to explore Fe (oxyhydr)oxide transformation and effects on phosphate sorption in soils with contrasting saturation and redox conditions. Synthetic Fe (oxyhydr)oxides (ferrihydrite, goethite and hematite) were coated onto quartz sand and either pre-sorbed with phosphate or left phosphate-free. The oxide-coated sands were mixed with natural organic matter, enclosed in mesh bags, and buried in and around a vernal pond for up to 12 weeks. Redox conditions were stable and oxic in the upland soils surrounding the vernal pond but largely shifted from Fe reducing to Fe oxidizing in the lowland soils within the vernal pond as it dried during the summer. Iron (oxyhydr)oxides lost more Fe (− 41% ± 10%) and P (− 43 ± 11%) when incubated in the redox-dynamic lowlands compared to the uplands (− 18% ± 5% Fe and − 24 ± 8% P). Averaged across both uplands and lowlands, Fe losses from crystalline goethite and hematite (− 38% ± 6%) were unexpectedly higher than losses from short range ordered ferrihydrite (− 12% ± 10%). We attribute losses of Fe and associated P from goethite and hematite to colloid detachment and dispersion but losses from ferrihydrite to reductive dissolution. Iron losses were partially offset by retention of solubilized Fe as organic-bound Fe(III). Iron (oxyhydr)oxides that persisted during the incubation retained or even gained P, indicating low amounts of phosphate sorption from solution. These results demonstrate that hydrologic variability and Fe (oxyhydr)oxide mineralogy impact Fe mobilization pathways that may regulate phosphate bioavailability.

Responsible Editor: Jeffrey A. Bird

Supplementary Information The online version contains supplementary material available at https://doi.org/10.1007/s10533-023-01094-z.

M. Barczok · N. Di Domenico · D. Singer
Department of Earth Sciences, Kent State University, Kent, OH, USA

C. Smith · L. Kinsman-Costello
Department of Biological Sciences, Kent State University, Kent, OH, USA

E. Herndon
Earth and Planetary Sciences, The University of Tennessee Knoxville, Knoxville, TN, USA

E. Herndon (✉)
Environmental Sciences Division, Oak Ridge National Laboratory, Oak Ridge, TN, USA
e-mail: herndonem@ornl.gov

Keywords Iron oxide · Phosphate · Redox · Vernal pond · X-ray absorption spectroscopy

Introduction

Iron oxide, hydroxide, and oxyhydroxide minerals (henceforth called Fe oxides) are an important and ubiquitous component of soils and sediments that regulate trace metal solubility (Tessier et al. 1985; Balint et al. 2015; Chen and Thompson 2018), organic matter stability (Kögel-Knabner et al. 2010; Lalonde et al. 2012; Herndon et al. 2017; Coward et al. 2017), and nutrient cycling (Roden and Edmonds 1997; Lambers et al. 2008; Ruttenberg and Sulak 2011; Chapin et al. 2002). For example, inorganic phosphate is the major form of phosphorus (P) used by all organisms for a wide variety of biological processes (Westheimer 1987; Vitousek et al. 2010), and Fe oxides are important geochemical controls on P solubility in soils, lakes, and oceans (Mortimer 1941; Patrick and DeLaune 1977; Caraco et al. 1990; Slomp et al. 1996; Wang et al. 2009; Herndon et al. 2019). Iron oxides strongly bind phosphate through mechanisms such as adsorption, coprecipitation, and occlusion (Khare et al. 2005; Chacón et al. 2006; Borch et al. 2007; Gu et al. 2020), removing the phosphate from solution and decreasing its availability to plants and microorganisms (Vitousek et al. 2010). Consequently, understanding controls and influences on phosphate adsorption to Fe oxides is vital to predict the bioavailability of P in a given ecosystem.

Iron oxides are sensitive to fluctuating redox conditions that vary with soil saturation. Soils moisture varies seasonally and in response to precipitation and may experience more extreme hydrologic fluctuations as the climate changes (USGCRP 2018). Iron oxides dissolve under reducing conditions that form in saturated soils and precipitate under oxidizing conditions that occur in drained soils. Reducing conditions develop as oxygen and other electron acceptors are depleted through microbial respiration more rapidly than they are supplied, leading to microbial (Bryce et al. 2018; Weber et al. 2006) or abiotic (Kappler et al. 2021) reduction of Fe(III) to Fe(II). As soils drain and become oxidizing, Fe(II) can be oxidized to Fe(III) by microorganisms, through reaction with O_2, or via surface-catalyzed oxidation of Fe(II) sorbed to Fe(III) oxides (Kappler et al. 2021; Bryce et al. 2018; Colombo et al. 2014). Formation and dissolution of Fe oxides consequently affect phosphate solubility. For example, a shift from oxic to anoxic conditions in laboratory incubation of tropical soils led to rapid but brief phosphate mobilization, presumably due to liberation from dissolving Fe oxides (Lin et al 2018). Adsorption of phosphate to Fe oxides is further determined by mineral properties and environmental factors such as pH. Iron oxides generally have positively charged surfaces under environmental conditions which attract anionic phosphate groups (e.g., $H_2PO_4^-$, HPO_4^{2-}) that form inner-sphere complexes with the mineral (Essington 2015). The capacity of Fe oxides to adsorb phosphate and the strength of this interaction is affected by crystallinity, with short-range-order (SRO) Fe oxides, such as ferrihydrite, having a higher adsorption capacity than more crystalline Fe oxides due to a higher surface area and more sorption sites (Ajmal et al. 2018; Mallet et al. 2013; Schwertmann and Cornell 2000).

The impacts of fluctuating redox conditions on Fe oxide crystallinity and resulting adsorption capacity for phosphate are inconsistent across natural environments. Predictions are made more difficult when considering varying effects of fluctuating redox on Fe oxide dissolution and reprecipitation. Organic matter content, initial Fe oxide composition, and leaching of Fe are all important factors that influence Fe oxide crystallinity and transformation. Some studies suggest that SRO Fe oxides accumulate under fluctuating redox conditions while other studies observe an increase in more crystalline phases (Thompson et al 2006; Vogelsang et al. 2016; Winkler et al. 2018; Bhattacharyya et al. 2018). Repeated redox oscillation has been thought to favor formation of SRO Fe oxides over crystalline Fe oxides (Moormann and Breemen 1978), as observed by Vogelsang et al. (2016) in organic-rich paddy soils. Reductive dissolution of Fe-oxides and subsequent oxidation of aqueous Fe(II) produces SRO Fe oxides that are slow to transform to more crystalline phases and are more accessible to repeated reduction by microorganisms that hinders crystallization. In addition, organic–mineral interactions in organic-rich systems can prevent the formation of more crystalline phases (Chen and Thompson 2018). Small amounts of organic matter can interfere with the particle size and crystalline order of ferrihydrite (Mikutta et al. 2008), resulting in smaller crystals with less crystalline order. Thus,

SRO Fe oxides accumulate under oscillating redox conditions in systems with high leaching of Fe and/or high concentrations of organic matter (Thompson et al. 2011). However, in closed systems where aqueous Fe(II) can accumulate near the mineral surface, Fe oxide crystallinity increases with repeated reduction–oxidation cycles as SRO Fe oxides transform into more crystalline phases in the presence of Fe(II) ions (Thompson et al. 2006; Tomaszewski et al. 2016). Electron transfer from the adsorbed Fe(II) to the Fe(III)-oxide results in the oxidation of Fe(II) to form an oxide with more defined crystalline structure (Handler et al. 2014; Schaefer et al. 2011; Williams and Scherer 2004) and/or destabilization of the ferrihydrite crystal lattice and subsequent precipitation of goethite or lepidocrocite (Pedersen et al. 2005).

In addition, the initial mineral composition of the soil Fe can play an important role in determining subsequent mineral transformation. In one study, soils enriched with either SRO or crystalline Fe oxides had contrasting responses to similar fluctuations in redox, leading to a convergence in mineralogy (Winkler et al. 2018). Soils enriched with SRO Fe oxides increased in crystallinity over time, both because crystalline phases were preserved as SRO phases dissolved and due to Fe(II)-facilitated re-crystallization. Soils enriched with crystalline Fe oxides decreased in crystallinity over time as aqueous Fe(II) released from reductive dissolution of crystalline Fe oxides re-precipitated and co-precipitated with organic matter to produce SRO Fe oxides (Winkler et al. 2018). These results and previous studies show the complexity and difficulty in predicting if Fe oxides will decrease or increase in crystallinity as redox fluctuates under variable saturation, consequently making it difficult to predict associated changes in phosphate solubility.

The objective of this study was to investigate changes in Fe oxide mineralogy and associated P sorption under contrasting redox regimes in and around a vernal pond. Vernal ponds are ephemeral water features characterized by seasonal hydrological changes, often ponding in the spring but drying up over the course of the summer, providing desired redox shifts that can be contrasted with surrounding unsaturated uplands. We previously observed strong correlations between dissolved Fe and phosphate in pore water at this vernal pond, indicating that Fe redox dynamics exert a strong control over phosphate solubility (Barczok et al. 2023). In this study, we incubated three synthetic Fe oxides with varying crystallinity (ferrihydrite, goethite, hematite) and P sorption (phosphate-added or phosphate-free) in either saturated vernal pond soils or in the unsaturated upland soils. We used X-ray Absorption Fine Structure (XAFS) spectroscopy and sequential extractions to investigate changes in Fe speciation and phosphate sorption over time. We hypothesized that Fe oxides incubated in the unsaturated upland would experience little to no change in Fe speciation or adsorbed phosphate while those incubated in the vernal pond soils (lowland) would dissolve to leach Fe and phosphate under reducing conditions. We also hypothesized that more crystalline phases would experience less Fe oxide dissolution and phosphate leaching than SRO Fe phases. Finally, we hypothesized that the shift from Fe reducing to Fe oxidizing conditions in lowland soils would lead to precipitation of SRO Fe oxides that partially offset net Fe loss and had a higher capacity for phosphate sorption than initial crystalline oxides. Geochemical properties of the soils from the study area are provided for context and to demonstrate environmental relevance of the mineral bag experiment.

Materials and methods

Site description

The study was conducted in Jennings Woods, a 30-ha hardwood temperate forest owned by Kent State University near Ravenna, Ohio, United States (41.177004°N,−81.205108°W) that has been unmanaged since 1973 (Fig. S1). Average summer (June to August) temperature and precipitation are 17.54 °C and 422 mm, respectively (NOAA 2021). Dominant soils are in the Chili loam series (fine-loamy, mesic Typic Hapludalf) and Geeburg-Glenford silt loam complexes (both Aquic Hapludalfs, but Geeburg is illitic and Glenford has a mixed clay mineralogy) (Blackwood et al. 2013).

Iron oxides were incubated inside mesh bags (“mineral bags”) in a vernal pond in Jennings Woods from May 10th, 2018 to August 2nd, 2018. The approximate length of the study pond was 20 m with a width of 10 m (Fig. 1). Polyvinyl chloride pipes were deployed in a randomized fashion in the upland soils

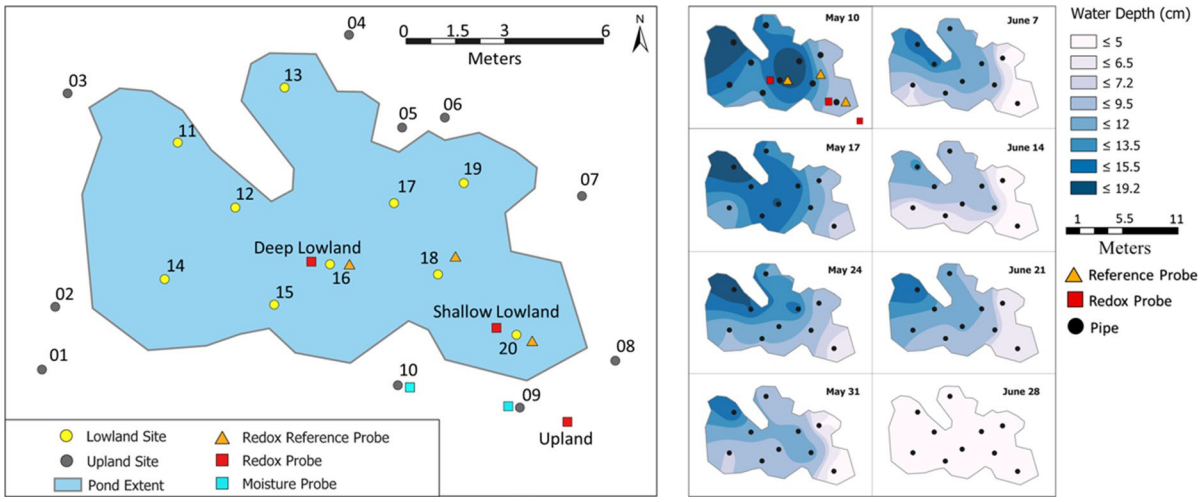

Fig. 1 (left) Extent of the vernal pond (delineated May 10th, 2018) and location of the PVC markers (numbered 1–20), redox reference probes, redox probes, and soil moisture probes. (right) Extrapolated weekly water depth in the pond from bag deployment (May 10th) to June 28th. Black markers indicate marker positions where water depths were measured. After June 28th to the end of the experiment (August 2nd), the pond remained unflooded. Map projection GCS WGS 1984 UTM 17N created with ArcGIS Pro 2020

around the pond (n = 10) and in the lowland soils in the pond (n = 10) and used as location references for site characterization and the incubation experiment.

Barczok et al. (2023) previously reported changes in surface water across the pond and in soil redox potential in the upland and lowland over the incubation period. Surface water depth decreased over the study period and was negligible on the shallow side of the vernal pond by June 28th and across the entire pond by July 5th (Figs. 1 and S2). Soil moisture in the upland was low (~ 10–20% volumetric water content) and declined by 36% over the study period, with periodic increases due to rainfall (Fig. S2). Soil redox patterns differed between the upland, shallow pond, and deep pond. Redox potential was stable and consistently high in the upland soil (722 ± 47 mV), indicating persistent Fe oxidizing conditions (considered to be > 300 mV following Thamdrup (2000)). Soil in the pond experienced variable redox conditions over space and time. The shallow lowland recorded Fe reducing conditions from June to July 13th (minimum $E_h = -93 \pm 36$ mV) and then transitioned to Fe oxidizing conditions from mid-July through early August (maximum $E_h = 687 \pm 83$ mV). The increase in redox potential in the shallow lowland did not directly coincide with the disappearance of surface water but instead took over 13 days to adjust to the higher redox potential that we would expect for unsaturated soils, as discussed by Barczok et al. (2023). Following an initial equilibration period during which Fe oxidizing conditions were recorded, the deep lowland declined into Fe reducing conditions and reached a minimum of 47 ± 20 mV.

Soil collection and characterization

Soil collection and characterization

Two soil cores were collected from the lowland in October 2018, approximately 5 cm from the two lowland redox probes (pipe 15 and pipe 20). Each core was retrieved with a 10 cm diameter soil auger in 5 cm increments from 0 to 20 cm depth and then at 10 cm increments from 20 to 60 cm depth. Soil was collected to 10 cm depth in the upland but attempts to core deeper were prevented by a dense root network. Core samples were air dried first and then oven dried at 40 °C until the soil reached constant mass.

Soil pH was measured by mixing 1 g of dried subsample with 10 mL of ultrapure water (Milli-Q, 18 MΩ) and measuring the pH of the solution after 10 min. To determine the size distribution of soil aggregates, dried soil was sieved to 1 mm, and the > 1 mm fraction was weighed. Soil aggregates and

particles < 1 mm were analyzed with a Malvern™ Mastersizer 2000 laser diffraction particle size analyzer equipped with a Hydro 2000MU manual inlet system. Size fractions are reported as the proportion of clay and silt size particles (< 0.053 mm), microaggregates (0.053 to 0.25 mm), small macroaggregates (0.25 to 1 mm), and large macroaggregates (> 1 mm). The morphology and chemical composition of soil particles and aggregates < 1 mm were evaluated using scanning electron microscopy (SEM) with energy dispersive spectroscopy (EDS) (Hitachi 3030TM series).

Subsamples of dried soil were ground into a fine powder in a ball mill with tungsten carbide grinding balls for five minutes (8000M SPEX). Milled soils were analyzed with X-Ray Fluorescence (XRF) analysis to determine major element concentrations. About 11 g of milled soil was mixed with 1.2 g of SPEX 3642 cellulose binder and then pressed into a pellet using a SPEX 3614 40 mm die set and Carver 25-ton hydraulic press. Milled soils were also analyzed with X-ray Diffraction (XRD) to determine mineral composition. Soils were analyzed as a loose powder at 15 Amps and 40 kV at a theta 2 angle of 3° to 90°. Fitting of the XRD spectra was done against the Crystallographic Open Database as a reference library. Relative abundance of minerals was determined by the Whole Pattern Powder Fitting method and a Rietveld Refinement with Rigaku's PDXL software. Carbon and nitrogen concentrations were measured on triplicate subsamples of milled powder (~ 5–7 mg) via combustion with an Elemental Analyzer (Costech ECS 4010).

Iron oxide incubation experiment

The incubation experiment consisted of 32 treatments with four factors. The first factor was Fe oxide mineralogy and included quartz sand coated with ferrihydrite (Fh), goethite (Gt), or hematite (Hm). Uncoated quartz sand was also incubated for comparison. The second factor was either phosphate addition or no phosphate addition. If phosphate was added, the treatment is called Fe-oxide-phosphate (for example Fh-phosphate) and if no phosphate was added, the treatment is called Fe-oxide-only (for example Fh-only). The third factor was landscape position and included incubations in either the unsaturated soils around the pond (upland) or in the periodically flooded soils in the vernal pond (lowland). The fourth factor was incubation time (i.e., 4 or 12 weeks). Incubated materials were compared to pre-incubation (0 week) materials that were prepared and analyzed in the same way but never incubated. Each factor was replicated five times to yield 160 total mineral bags; however, experimental replicates were combined and homogenized to obtain sufficient mass for analysis, as described below.

Iron oxide synthesis

Iron oxide-coated sand used in this experiment was prepared and synthesized in the laboratory before deployment in the field. Ferrihydrite was synthesized after Brooks et al. (1996) by preparing a 0.33 M $FeCl_3$ solution in ultrapure water. The solution was then titrated with 1.0 M NaOH to pH 7.5 within 5–10 min under constant stirring to prevent the formation of akageneite or goethite (Hansel et al. 2003). Goethite was synthesized after Schwertmann and Cornell (2000) by preparing a 0.33 M $FeCl_2$ solution with deoxygenated ultrapure water in an N_2/H_2 gas mixture atmosphere (Coy anaerobic chamber). The ultrapure water was deoxygenated by purging it with N_2 gas while boiling for one hour. To precipitate goethite, 110 mL 1 M $NaHCO_3$ was added to the $FeCl_2$ solution outside the anerobic chamber under constant stirring. Air was added to the constantly stirred solution at a rate of 30–40 mL per minute for 48 h. This method produces sub-micron, elongated goethite crystals (Schwertmann and Cornell 2000). Hematite was synthesized after Schwertmann and Cornell (2000) by preparing a 1 M $Fe(NO_3)_3$ solution in ultrapure water. The solution was then slowly titrated, at a rate of 1–2 drops a second with a burette, into boiling ultrapure water in a beaker under constant stirring. The solution was allowed to boil for 3–4 h and then cooled in a fume hood overnight. This method produces hematite crystals approximately 7–10 nm in diameter (Schwertmann and Cornell 2000).

Mineral slurries were centrifuged for 20 min at 4000 rcf. Supernatant was discarded and the mineral precipitates were rinsed three times by addition of ultrapure water and subsequent centrifugation. The rinsed mineral slurries were then either frozen and stored in a freezer at − 17 °C or immediately used to coat quartz sand. A subsample of each mineral was freeze-dried and confirmed to be 2-line ferrihydrite, goethite, or hematite by powder x-ray diffraction

using a MiniFlex 6G Benchtop X-Ray Diffractometer (Rigaku) with a D/teX Ultra2 detector operated with a Cu X-ray tube (λ = 1.5406 Å) at 40 kV and 15 mA (Fig. S3).

Quartz sand (Lane Mountain Company, Silica Sand) was purchased and sieved to isolate the 115–165 mesh size particles (125–212 µm), which were determined to be 99% SiO_2 by X-ray fluorescence (XRF, Epsilon 3 XLE Benchtop Energy Dispersion XRF) powder analysis. To coat the sand, each Fe oxide slurry was mixed with sand and allowed to dry in a drying oven at 105 °C for 24 h. The coated sand was washed with ultrapure water three times, dried for 24 h at 105 °C, then stored at − 17 °C. A quartz control consisting of only quartz sand and no added Fe oxides was washed three times and dried at 105 °C for 24 h and stored in a freezer at − 17 °C.

Phosphate sorption

To generate Fe-oxide-phosphate treatments, phosphate was adsorbed to Fe oxide coated-sand and quartz sand following a protocol developed by Bache and Williams (1971). Approximately 200 g of quartz sand or Fe oxide-coated sand were added to 2 L of 75 mg-P L^{-1} (as potassium phosphate monobasic) in 0.01 M KCl solution and stirred for 24 h. After 24 h, the sand was separated from the solution by filtering it through a ~ 20–25 µm pore size cellulose filter paper and air-dried (Bache and Williams 1971). Phosphate remaining in solution was quantified on a UV–Visible Spectrophotometer (Shimadzu UV-1800) with a PhosVer3 reagent (Hach). Briefly, 10 mL of the solution was mixed with PhosVer 3 reactant, shaken for 30 s and then allowed to react for two minutes. After two minutes, the solution was analyzed at 880 nm wavelength on the UV–Vis to determine phosphate concentration by comparison with a five-point calibration curves prepared using standard solutions. Initial sorption of phosphate to the synthesized Fe oxides was calculated as the difference in PO_4^{3-} concentration from the pre- to the post-sorption solutions.

Mineral bag preparation and deployment

Coated and uncoated sand (8 g) were mixed with organic peat (2 g) and sealed in 5 µm nylon mesh bags with a heat sealer. Organic soil (commercially available organic peat moss with < 0.5% Fe determined by x-ray fluorescence) was included in the mineral bags to provide an organic substrate that is more similar to forested surface soils than coated quartz sand alone. Mineral bags were autoclaved to sterilize and stored in a freezer at − 17 °C for up to two weeks until deployment. Fishing line was used to secure each bag to a PVC marker in the field. PVC location markers placed in the upland soils (n = 10) and in the lowland pond soils (n = 10) (Fig. 1) were randomly designated for bag retrieval after 4 weeks (T1; n = 5) or after 12 weeks (T2; n = 5). Around each marker, one bag from each mineral-phosphate combination (8 total) was buried at approximately 5 cm depth in the soil (excluding the litter layer). Additional bags from each treatment were not buried and instead were stored in the laboratory and kept as time zero (T0) samples.

Post-experiment analyses

Mineral bag collection

Upon retrieval, mineral bags were quickly transferred into an airtight container (MGC, Anaerobic Pack System) containing a N_2/H_2 atmosphere and an oxygen consuming catalyst that generated carbon dioxide (MGC, Pack-Anaero). Bags were then transported to Kent State University and stored in an anaerobic chamber (1.5% H_2, 98.5% N_2, < 0.1 ppm O_2, Coy Laboratories, Inc.). Incubated materials from experimental replicates (n = 5) were combined and homogenized in the anerobic chamber to yield sufficient mass for multiple analyses. Thus, each treatment represents a composite of five environmental replicates. Approximately 15 g of homogenized material were subsampled, frozen, and then freeze-dried in preparation for geochemical analyses. Incubated material pH was determined by weighing 1 g of freeze-dried subsample from each treatment, mixing it with 10 mL of ultrapure water, and measuring the pH of the solution after 10 min.

Sequential extraction

Sequential P and Fe extractions were performed to evaluate loss or gain of water-soluble and dithionite-soluble Fe and P, which represent loosely sorbed bioavailable P and Fe or P and Fe associated with Fe oxides, respectively. To obtain the water-soluble fraction, deoxygenated ultrapure water was prepared

by purging it with N_2 gas while bringing the water to a boil for about two hours. One gram of freeze-dried sample was transferred to a 50 mL centrifuge tube inside an anaerobic chamber and mixed with 25 mL of cooled deoxygenated ultrapure water. The mixture was put on an end-over-end rotator inside the anaerobic chamber and mixed for 1 h at 250 rpm. After 1 h, the centrifuge tube was removed from the anaerobic chamber and centrifuged for 20 min at 4000 rcf. The supernatant was filtered through a 0.45 µm syringe filter inside the anerobic chamber and stored in a new centrifuge tube. The remaining pellet was rinsed with 25 ml of deoxygenated ultrapure water, centrifuged for another 10 min at 4000 rcf, and the supernatant was filtered and added to the original extract. The extract was acidified with 1 mL of 1 M sulfuric acid, stored in a fridge, and analyzed on a UV–Vis for soluble reactive phosphorus (i.e., hereafter referred to as phosphate; detection limit converts to < 0.016 µmol PO_4^{3-} g^{-1}) within two weeks and on ICP-OES for Fe (< 0.005 µmol Fe g^{-1}). Calibration curves were prepared from calibration standards in matrix-matched solutions, i.e., ultrapure water or diluted dithionite solutions acidified with sulfuric acid. The remaining sample pellet was stored in the fridge less than seven days prior to the second extraction step.

Second, a dithionite extraction was performed to extract Fe and P associated with Fe oxides following an extraction scheme adapted from Paludan and Jensen (1995). A 0.11 M bicarbonate-buffered sodium dithionite solution was prepared in deoxygenated ultrapure water inside the anaerobic chamber less than 24 h before the dithionite extraction. All extraction steps were also performed in the anerobic chamber. 25 mL of sodium dithionite solution was added to the remaining pellet from the water-soluble extraction and mixed for 1 h on an end-over-end rotator at 250 rpm. The slurry was then centrifuged for 20 min at 4000 rcf, and the supernatant was poured into a plastic bottle. The pellet was then sequentially rinsed with 25 mL dithionite solution and 25 mL ultrapure deoxygenated water, and the rinse solutions were combined with the original supernatant following centrifugation for 10 min at 4000 rcf. The remaining steps were performed outside the anaerobic chamber. The combined supernatant was vacuum filtered through a A/E filter in a filter tower. Filtered solutions were then aerated for 1 h before being acidified with 250 µL of concentrated sulfuric acid. The extract was stored in a fridge and analyzed on a UV–Vis for phosphate within two weeks and on ICP-OES for Fe. Errors for sequential extractions were calculated based on the relative standard error of triplicate extractions of each mineral (Table S1) for each individual treatment (for example, Fh-phosphate) or as standard error of the mean for the average of multiple treatments.

Element concentrations in extract solutions were normalized to the dry mass of material in the incubated bags to yield element concentrations in the bagged minerals (µmol g^{-1}). P:Fe ratios (µmol P (mmol Fe)$^{-1}$) were calculated by dividing dithionite-soluble P (µmol g^{-1}) by dithionite-soluble Fe (mmol g^{-1}).

P:Fe-oxide ratios (µmol P (mmol oxide-Fe)$^{-1}$) were calculated as follows:

$$\mathrm{P:Fe-oxide} = \frac{C_{\mathrm{P,dithionite}}}{f_{\mathrm{Fe,oxide}} C_{\mathrm{Fe,dithionite}}},$$

where $C_{\mathrm{P,dithionite}}$ is the concentration of dithionite-soluble P (µmol g^{-1}), $C_{\mathrm{Fe,dithionite}}$ is the concentration of dithionite-soluble Fe (mmol g^{-1}), and $f_{\mathrm{Fe,oxide}}$ is the fraction of total Fe contained in Fe-oxides (Fh, Gt, and Hm combined) determined by linear combination fits from EXAFS (see below). The P:Fe-oxide calculation was performed to remove the contribution of organic-bound Fe from dithionite-soluble Fe and isolate the amount of Fe in Fe-oxides. Error for all P:Fe ratios were calculated as propagated error from dithionite-soluble P and Fe.

X-ray absorption fine-structure and micro-X-ray fluorescence spectroscopy

X-ray absorption fine-structure (XAFS) spectroscopy was used to analyze changes in Fe speciation during incubation. XAFS was measured at 12-BM and µ-XRF was measured at 13-ID-E at the Advanced Photon Source (APS) at Argonne National Laboratory (Chicago, IL, USA). Samples for XAFS were prepared as a thin powder on Kapton tape inside an anaerobic chamber, transported to APS in N_2/H_2 atmosphere filled air-tight containers, and mounted on Teflon sample holders. Additional analyzed reference materials included synthesized ferrihydrite, hematite, and goethite powders, and commercial Fe(III) chloride, Fe(II) chloride, Fe(III) nitrate, Fe(III) citrate,

Fe(II) oxalate, Fe(III) oxalate and Fe(III) phosphate powders. Reference spectra for 2-line ferrihydrite, goethite, and hematite were retrieved from a XAFS Fe database reported by Advanced Lightsource 10.3.2. XAFS spectra were collected from − 150 eV to + 547 eV around the Fe K-edge (~ 7112 eV) with a 500 µm beam that yields 4×10^{11} photons s^{-1} at 12 keV. Detectors included a N_2-filled Ionization Chamber for transmission and a Canberra 13 element detector for fluorescence. Three to five scans were taken from different locations (about 1 mm apart) on each sample to account for any heterogeneity and then merged into one spectrum using the XAS data processing software Athena (version 0.9.26; Ravel and Newville 2005). Reference spectra of an Fe foil collected in line with the samples were shifted to align with the reference Fe foil ($E_0 = 7110.6$ eV) spectrum reported in the Fe reference library. Transmission spectra were used where possible; fluorescence spectra were used where Fe concentrations were too low to yield quality transmission data. All spectra are provided in the supporting information (Tables S2 and S3).

Linear combination fits (LCFs) were performed in EXAFS ($k^2\chi(k)$) from 3 to 10 $Å^{-1}$ using reference spectra for ferrihydrite, goethite, hematite, ferric citrate, ferric oxalate, and ferric phosphate within Athena (Kiczka et al. 2011; Sjöstedt et al. 2013; Giannetta et al. 2020) to determine changes in Fe speciation over time. Best fits were determined as the spectral combination reporting the lowest chi-square number using the lowest number of reference spectra. That is, additional components were not included unless they improved the fit by > 10%. Fits from 3 to 10 $Å^{-1}$ and in ($k^2\chi(k)$) gave similar results but a lower chi-square error compared to fits from 3 to 12 $Å^{-1}$ or in ($k^3\chi(k)$) and were therefore reported here; however, fitting with $k^3\chi(k)$ and to k > 10 $Å^{-1}$ are generally preferred to resolve spectral differences (O'Day et al. 2004). Spectra were not included unless they improved the chi-square error by more than 20%. Mineral transformation was calculated as the percent change between the initial and final mineral composition of each treatment. For example, lowland Hm-phosphate contained 100% Hm initially and 46% Hm after 12 weeks, giving a mineral transformation of 54%.

Micro-x-ray fluorescence (µ-XRF) was used to confirm phosphate sorption to Fe oxides. A subsample from the pre-incubation Fh-phosphate material was embedded in epoxy and prepared as 30 µm thick double-sided-polish thin section mounted on Suprasil 2A Quartz glass (Spectrum Petrographics, Inc., Vancouver, WA) for µ-XRF mapping. The thin section was analyzed at 13-ID-E at APS (Newville et al. 1999). The beam was focused to 2 µm × 2 µm using a Pt-coated Kirkpatrick–Baez (K–B) focusing optics system (Xradia, Zeiss Microscopy, Pleasanton, CA). Maps were collected at 7136 eV with a dwell time of 20 ms per pixel. Fluorescence maps were analyzed and processed using the software package Larch v.0.9.46 (Newville 2013). Regions of interest were defined for Si (1.5 to 1.9 keV), P (1.9 to 2.1 keV), and Fe (6.1 to 6.7 keV) to generate a tri-color map and plot correlations of P with Si and Fe.

Statistical analyses

Two-way analysis of variance (ANOVA) tests were performed in OriginPro® to determine the effects of initial mineralogy and landscape position (upland or lowland) on Fe speciation, water-soluble Fe, dithionite-soluble Fe, dithionite-soluble P, and P:Fe ratios over the incubation period ($\alpha = 0.05$). Means comparisons were determined using a post-hoc Tukey test. Water- and dithionite-soluble Fe and P were normalized to their initial concentrations and evaluated as % change for better comparison across different minerals. Values were grouped across time (4 and 12 weeks) to evaluate changes in P within each phosphate-addition treatment (P added or no P added) and across both time and phosphate-addition to evaluate changes in Fe since these factors were either not significant or marginally significant, as described in the results. Goethite and Hm, which exhibited similar patterns, were combined as "crystalline oxides" and compared to Fh.

Results

Soil properties

Soil cores from the shallow and deep lowland were similar in composition (Fig. S4). Soil pH was low (pH 3.5–3.6) in all surface soils and increased with depth but remained below pH 4.5 (Table S4). Surface soils were organic-rich in the shallow lowland

(C = 15.5 ± 0.2 wt%, N = 1.2 ± 0.0 wt%) and deep lowland (C = 13.5 ± 0.4 wt%, N = 1.1 ± 0.0 wt%) and organic-poor at depths > 10 cm (< ~ 3–4 wt% C; < ~ 0.3–0.4 wt% N). Soil cores in both the shallow and deep lowland were dominated by the clay, silt, and large macroaggregates with smaller fractions of microaggregates and small macroaggregates (≤ 10%) (Fig. S5). Crystalline mineralogy was dominated by quartz, clays (vermiculite and kaolinite), K-feldspar, plagioclase feldspar, and mica. Iron (oxyhydr)oxides were not detected with XRD, as expected for poorly crystalline minerals. However, total Fe concentrations determined by XRF ranged from 2.0 to 6.2% and were generally higher in soils deeper than 30 cm (Fig. S4).

Surface soils (< 10 cm) contained high proportions of organo-mineral aggregates (> 300 µm) while deeper soils were organic-poor and comprised of mineral grains (Fig. S6). In surface soils, clay- and silt-sized grains in the aggregates contained mostly Si and O with lesser contributions of Al and K, consistent with quartz and aluminosilicates. Iron was diffusely distributed across the aggregates rather than associated with Si-rich grains, consistent with the occurrence of Fe (oxyhydr)oxides associated with organic matter or organic-bound Fe species. Deeper soils (50–60 cm) were dominated by < 50 µm elongated clay and silt grains and larger > 100 µm angular grains and aggregates. Both small and large grains contained O, Si, Al, Mg, and K, indicating quartz and aluminosilicate minerals. Iron in the deeper soils was enriched in association with select Si-bearing grains rather than being distributed across all grains, consistent with its occurrence as Fe (oxyhydr)oxide coatings on quartz and clay particles.

Pre-incubation Fe oxide properties

Initial Fe oxides coated onto the quartz sand were confirmed as Fh (100%) and Hm (100%), although Gt contained a small quantity of Fh (15–18%) (Table S6). Previous studies using the same method of Gt synthesis have also noted that this method results in less crystalline Gt with high surface area and some formation of Fh (Hansel et al. 2003; Guzman et al. 1994). Initial average Fe oxidation states for all minerals closely resembled Fe(III) reference spectra and were not observed to change over time in any treatments, indicating low or negligible retention of Fe(II) following Fe reduction (Fig. S7).

Initial dithionite-soluble Fe concentrations differed amongst treatments, with Fh treatments having the highest Fe concentrations and quartz having the lowest (Table 1). Dithionite-soluble Fe is thus primarily reported as a percentage change over time in order to better compare across treatments. Reaction with the phosphate solution during preparation of the Fe-oxide-phosphate treatments caused small to moderate loss of Fe: that is, Fh (2% loss), Gt (35% loss), and Hm (22% loss) all had less initial Fe in the Fe-oxide-phosphate treatments than the Fe-oxide-only treatments (Table 1). Excess phosphate can promote dispersion of Fe-oxide colloids such as goethite by decreasing their surface charge (Ilg et al. 2008), which may explain Fe loss in Gt and Hm treatments during phosphate sorption.

Initial dithionite-soluble P concentrations, reported here as µmol P (as phosphate) per mmol Fe, also differed amongst Fe oxides and decreased from Fh (76.2 ± 1.7 µmol P (mmol Fe)$^{-1}$) to Gt (55.5 ± 3.0 µmol P (mmol Fe)$^{-1}$) to Hm (53.5 ± 4.6 µmol P (mmol Fe)$^{-1}$) (Table S5). These differences resulted in initial dithionite-soluble phosphate per bag that decreased in the order Fh-phosphate (11.82 ± 0.24 µmol P g^{-1}), Gt-phosphate (3.58 ± 0.07 µmol P g^{-1}), to Hm-phosphate (2.73 ± 0.22 µmol P g^{-1}) (Table 2). Quartz-phosphate, which contained little Fe, had comparatively low phosphate (0.40 ± < 0.01 µmol P g^{-1}). The amount of P present as dithionite-soluble P at time zero is equivalent to the amount of P removed from solution during the sorption process. No phosphate remained in solution following sorption to Fh while substantial phosphate remained in solution for Gt, Hm, and quartz sand, indicating that ferrihydrite was not fully saturated with phosphate.

We confirmed that added phosphate was predominantly associated with Fe oxides instead of the quartz sand or peat using µ-X-Ray fluorescence (Fig. S8). The Fe-oxides completely coated some of the smaller quartz grains, but the coatings were sporadic rather than uniformly present on all grains. This observation supports the assumption that phosphate is primarily adsorbed to the Fe-oxides and not the quartz sand or organic peat as there is no overlap of Si and P on the non-coated grains.

Table 1 Water-soluble and dithionite-soluble Fe (μmol g^{-1}) extracted from pre-incubation (week 0) and post-incubation (weeks 4 and 12) materials (minerals + organic matter)

Mineral treatment	Location	PO_4^{3-} Addition	Water-soluble Fe (μmol Fe g^{-1})			Dithionite-soluble Fe (μmol Fe g^{-1})		
			Week 0	Week 4	Week 12	Week 0	Week 4	Week 12
Quartz	Upland	Yes	< DL	< DL	< DL	0.82 ± 0.02	0.45 ± 0.02	0.64 ± 0.02
	Lowland	Yes	< DL	0.008 ± 0.09	0.016 ± 0.09	0.82 ± 0.02	0.88 ± 0.02	1.46 ± 0.02
	Upland	No	< DL	< DL	< DL	0.81 ± 0.02	1.16 ± 0.02	1.19 ± 0.02
	Lowland	No	< DL	0.050 ± 0.09	0.041 ± 0.09	0.81 ± 0.02	2.19 ± 0.02	0.59 ± 0.02
Ferrihydrite	Upland	Yes	0.202 ± 0.03	0.049 ± 0.01	0.087 ± 0.01	155.23 ± 1.55	171.39 ± 1.71	131.31 ± 1.31
	Lowland	Yes	0.202 ± 0.03	0.119 ± 0.02	0.137 ± 0.02	155.23 ± 1.55	144.10 ± 1.44	168.12 ± 1.68
	Upland	No	0.117 ± 0.02	0.071 ± 0.01	0.098 ± 0.02	158.70 ± 1.59	178.04 ± 1.78	157.71 ± 1.58
	Lowland	No	0.117 ± 0.02	0.085 ± 0.01	0.142 ± 0.02	158.70 ± 1.59	143.44 ± 1.43	96.17 ± 0.96
Goethite	Upland	Yes	0.034 ± 0.01	0.099 ± 0.01	0.063 ± 0.01	64.56 ± 3.23	40.61 ± 2.03	56.64 ± 2.83
	Lowland	Yes	0.034 ± 0.01	0.166 ± 0.01	0.225 ± 0.02	64.56 ± 3.23	33.82 ± 1.69	25.15 ± 1.26
	Upland	No	0.033 ± 0.01	0.368 ± 0.03	0.060 ± 0.01	99.40 ± 4.97	82.39 ± 4.12	81.05 ± 4.05
	Lowland	No	0.033 ± 0.01	0.138 ± 0.01	0.193 ± 0.01	99.40 ± 4.97	78.19 ± 3.91	42.56 ± 2.13
Hematite	Upland	Yes	0.048 ± 0.01	0.224 ± 0.06	0.151 ± 0.04	51.07 ± 1.53	48.02 ± 2.88	33.35 ± 1.00
	Lowland	Yes	0.048 ± 0.01	0.208 ± 0.06	0.182 ± 0.05	51.07 ± 1.53	36.00 ± 2.16	28.78 ± 0.86
	Upland	No	0.066 ± 0.02	0.147 ± 0.04	0.301 ± 0.08	65.67 ± 1.97	58.87 ± 3.53	49.36 ± 1.48
	Lowland	No	0.066 ± 0.02	0.266 ± 0.07	0.276 ± 0.08	65.67 ± 1.97	42.65 ± 2.56	31.68 ± 0.95

Error values (±) represent either methodological uncertainty obtained from extractions of three subsamples from each Fe oxide treatment (Table S1) or analytical error for quartz treatments

Table 2 Water-soluble and dithionite-soluble reactive P (SRP) (μmol g^{-1}) extracted from pre-incubation (week 0) and post-incubation (weeks 4 and 12) materials (oxide-coated sand + natural organic matter)

Mineral treatment	Location	PO_4^{3-} addition	Water-soluble P (μmol SRP g^{-1})			Dithionite-soluble P (μmol SRP g^{-1})		
			Week 0	Week 4	Week 12	Week 0	Week 4	Week 12
Quartz	Upland	Yes	0.51 ± 0.01	0.12 ± 0.01	0.07 ± 0.01	0.40 ± 0.01	0.68 ± 0.01	0.44 ± 0.01
	Lowland	Yes	0.51 ± 0.01	0.03 ± 0.01	< DL	0.40 ± 0.01	0.53 ± 0.01	0.54 ± 0.01
	Upland	No	< DL	0.03 ± 0.01	0.05 ± 0.01	0.99 ± 0.01	0.45 ± 0.01	1.33 ± 0.01
	Lowland	No	< DL	0.08 ± 0.01	< DL	0.99 ± 0.01	0.63 ± 0.01	0.44 ± 0.01
Ferrihydrite	Upland	Yes	0.04 ± 0.01	0.09 ± 0.01	0.05 ± 0.01	11.82 ± 0.24	9.86 ± 0.20	11.49 ± 0.23
	Lowland	Yes	0.04 ± 0.01	0.04 ± 0.01	0.02 ± 0.01	11.82 ± 0.24	10.10 ± 0.20	10.87 ± 0.22
	Upland	No	< DL	< DL	< DL	0.48 ± 0.01	0.62 ± 0.01	0.85 ± 0.02
	Lowland	No	< DL	< DL	0.02 ± 0.01	0.48 ± 0.01	0.78 ± 0.02	0.95 ± 0.02
Goethite	Upland	Yes	0.33 ± 0.02	0.12 ± 0.01	0.13 ± 0.01	3.58 ± 0.07	1.84 ± 0.04	2.62 ± 0.05
	Lowland	Yes	0.33 ± 0.02	0.07 ± 0.01	< DL	3.58 ± 0.07	1.35 ± 0.03	1.04 ± 0.02
	Upland	No	< DL	< DL	0.03 ± 0.01	0.59 ± 0.01	0.58 ± 0.01	0.87 ± 0.02
	Lowland	No	< DL	< DL	< DL	0.59 ± 0.01	0.90 ± 0.02	0.75 ± 0.02
Hematite	Upland	Yes	0.32 ± 0.05	0.09 ± 0.01	0.09 ± 0.01	2.73 ± 0.22	2.10 ± 0.17	2.09 ± 0.17
	Lowland	Yes	0.32 ± 0.05	0.05 ± 0.01	< DL	2.73 ± 0.22	1.29 ± 0.10	0.99 ± 0.08
	Upland	No	< DL	< DL	0.04 ± 0.01	0.56 ± 0.04	0.50 ± 0.04	0.46 ± 0.04
	Lowland	No	< DL	0.02 ± 0.01	0.11 ± 0.02	0.56 ± 0.04	0.59 ± 0.05	1.08 ± 0.09

Error values (±) represent either methodological uncertainty obtained from extractions of three subsamples from each Fe oxide treatment (Table S1) or analytical error for quartz treatments

Pre-incubation pH of the sand + peat mixture (4.1 ± 0.2) was only slightly higher than soil pH and had no change in the lowland (4.1 ± 0.1) but a small decrease in the upland (3.7 ± 0.1) following incubation (Table S5).

Iron mobilization during mineral incubation

The mineral bags lost more Fe when incubated in the lowland than in the upland. Averaged across all mineral and phosphate combinations at 12 weeks, lowland samples (n = 6) lost 41 ± 10% dithionite-soluble Fe while upland samples (n = 6) lost only 18 ± 5% dithionite-soluble Fe (Table 1; p = 0.061). Crystalline oxides (Gt and Hm) lost more Fe than ferrihydrite. Averaged across upland and lowland positions, decreases in dithionite-soluble Fe were larger for Gt and Hm (− 38 ± 6%; n = 8) than for Fh (− 12 ± 10%; n = 4) (p = 0.018). Averaged across all minerals and landscape positions, Fe loss after 12 weeks (− 29 ± 6%) was higher than 4 weeks (− 17 ± 5%) (p = 0.03; n = 24), but the differences in Fe loss from 4 to 12 weeks within each mineral treatment were not significant (p > 0.05) (Fig. S9). Also, differences in Fe loss between mineral-phosphate and mineral-only treatments were not significant (n = 24; p = 0.75); therefore, values are subsequently presented as averages across phosphate treatments and across time to evaluate effects of mineralogy and landscape position on Fe loss and speciation.

In the lowland, Gt (− 47 ± 9%) and Hm (− 40 ± 5%) treatments (n = 8) lost more dithionite-soluble Fe than Fh treatments (− 12 ± 11%; n = 4) (p = 0.003) (Fig. 2) (Table 1). The quartz treatment gained small amounts of Fe (+ 0.47 ± 0.35 µmol Fe g^{-1}), but these gains were much smaller than changes measured for the Fe oxides. In the upland, dithionite-soluble Fe decreased in Gt (− 21 ± 5%) and Hm (− 19 ± 7%) treatments (n = 8) but remained unchanged in Fh treatments (1.6 ± 6.4%; n = 4). The quartz treatments had no consistent change in dithionite-soluble Fe over time (0.05 ± 0.19 µmol Fe g^{-1}).

Water-soluble Fe was low in all treatments and often 10 × to 1000 × lower than dithionite-soluble Fe (Table 1). For both upland and lowland positions, water-soluble Fe decreased in the Fh treatments (− 113 ± 67% and − 30 ± 19%, respectively) but increased in the Gt and Hm treatments (129 ± 37% and 244 ± 70%, respectively) (Fig. 2). Mineralogy (p < 0.001) was a significant factor affecting water-soluble Fe, but landscape position was not. Water-soluble Fe was below detection in the initial quartz material (t = 0) and remained below or close to the detection limit over time (Table 1).

Iron transformation during incubation

Changes in Fe speciation over time were evaluated by comparing Fe K-edge EXAFS spectra for the incubated material to the initial, pre-incubation material (Fig. 3). Spectra for initial Fh-, Gt-, and Hm-containing material exhibited two distinct peaks at ~ 7.6 and ~ 8.7 $Å^{-1}$, consistent with Fe-oxides (O'Day et al. 2004), that decreased in amplitude from Hm to Gt to Fh. Spectra for Fe-oxide-only and Fe-oxide-phosphate treatments were indistinguishable within each mineral class (Fig. 3), indicating that phosphate sorption had no observable effects on initial Fe speciation. Iron transformation during incubation was primarily indicated by shifts and decreasing amplitudes of the two indicated peaks, particularly in the Hm treatments and in the lowlands. These spectral changes are consistent with an increasing proportion of organic-bound Fe(III), which exhibits a single peak at ~ 8 $Å^{-1}$ in lieu of the two peaks associated with Fe-oxides (Karlsson and Persson 2010).

Linear combination fits to EXAFS spectra were performed to quantify Fe transformation in each treatment (Table S6; Fig. S10). Iron transformation was more pronounced in the lowland treatments for all Fe-oxides (47% ± 7%) compared to the upland treatments (6% ± 4%) after 12 weeks (p < 0.001), but differences between initial mineral classes were not significant. Although most lowland treatments lost Fe and experienced > 40% Fe transformation by 12 weeks, Fh-phosphate gained Fe (Table 1) and experienced relatively minor transformation (14%). Iron transformation was dominated by loss of Fe oxides and formation of organic-bound Fe(III) but differed between mineral-only and mineral-phosphate treatments (Fig. 4). Specifically, Fe composition shifted towards a mix of organic-bound Fe(III) and Gt in the Fe-oxide-only treatments but towards only organic-bound Fe(III) in the Fe-oxide-phosphate treatments (Fig. 4; Table S6). Minor to negligible formation of organic-bound Fe(III) occurred in the upland, with

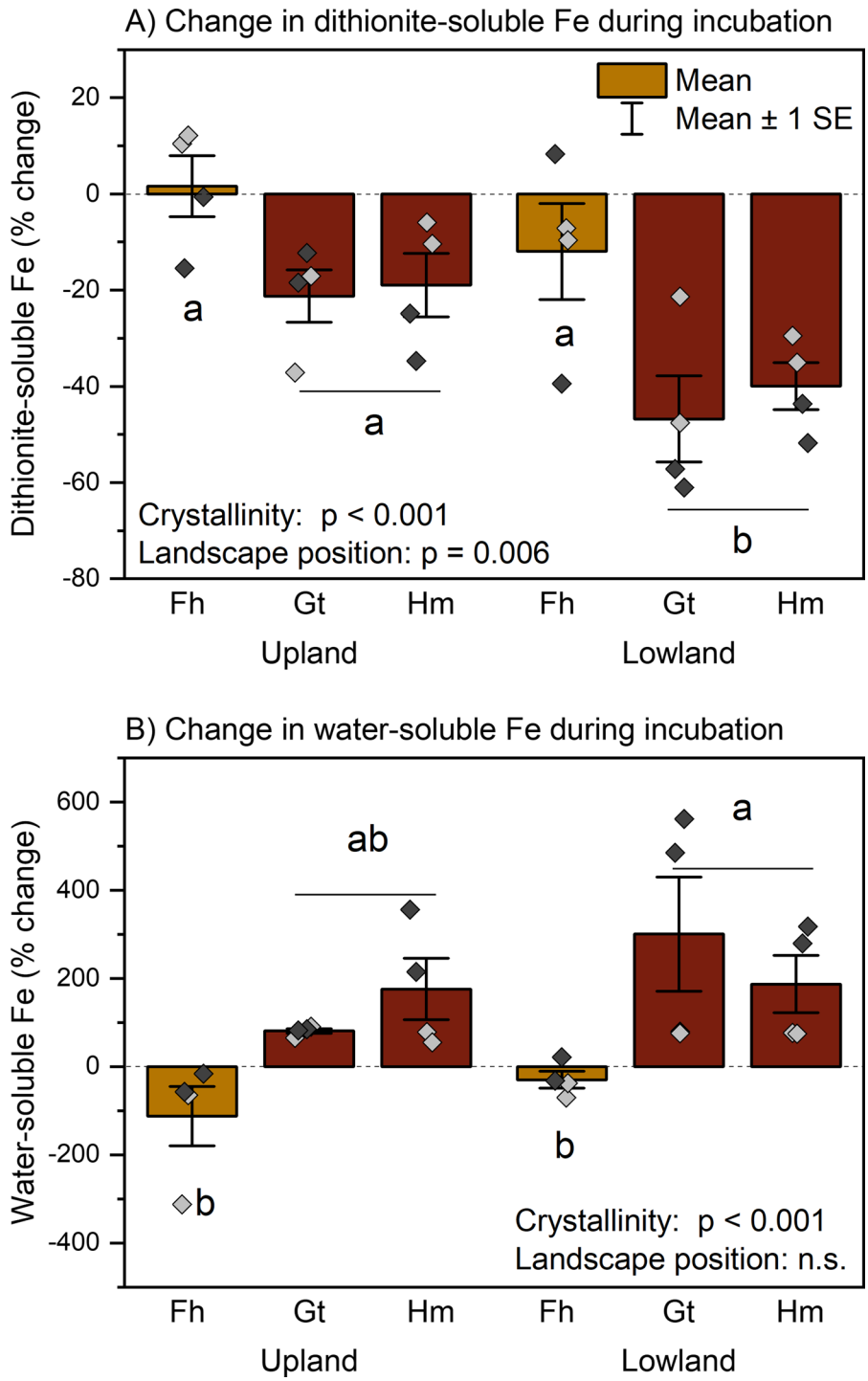

Fig. 2 Changes (%) in **A** dithionite-soluble Fe and **B** water-soluble Fe in incubated material relative to the initial pre-incubation material. Each bar represents the mean (± standard error) across phosphate treatments (Fe-oxide-only and Fe-oxide-phosphate) and incubation time (4 and 12 weeks) for each mineral and landscape position combination. Symbols indicate individual samples and are light grey for the 4 week incubation and dark grey for the 12 week incubation. The effects of landscape position (upland vs lowland) and crystallinity (Fh vs Gt + Hm) are denoted by p-values determined using two-way ANOVA. Different letters indicate significant differences between means associated with each crystallinity/landscape position combination, as determined using a post-hoc Tukey test to $\alpha = 0.05$

Gt treatments gaining the most organic-bound Fe(III) (12–14%) after 12 weeks. The Gt-phosphate treatment also contained minor Hm (12%) (Table S6).

Phosphate mobilization during mineral incubation

Changes in dithionite-soluble P (as phosphate) during incubation followed the same trends as

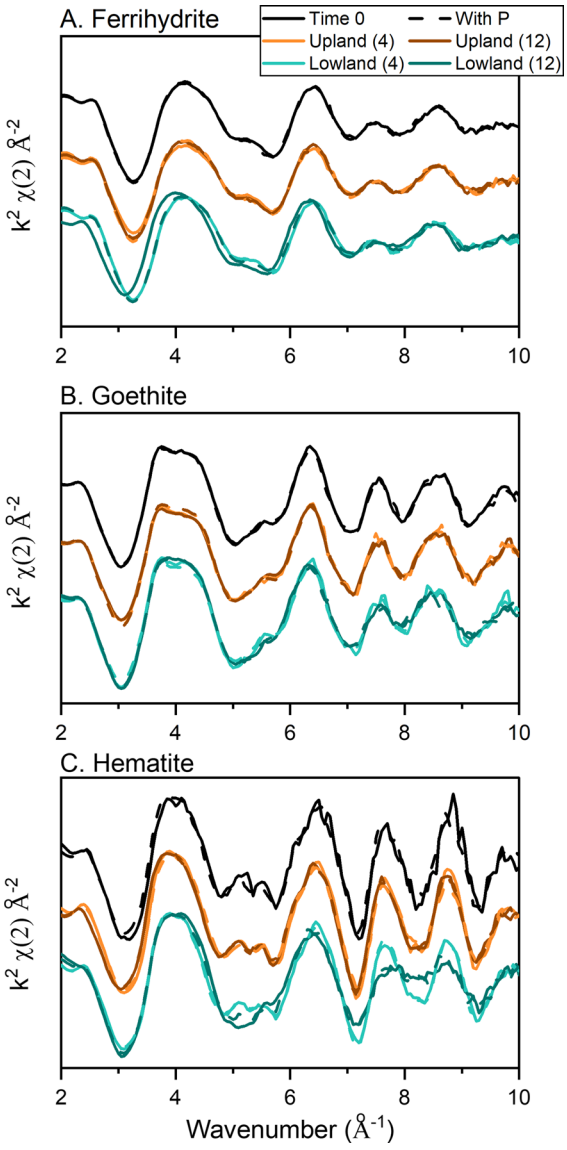

Fig. 3 Iron K-edge EXAFS spectra for Fe-oxide-only (solid lines) and Fe-oxide-phosphate (dashed lines) treatments incubated in the upland (orange) or lowland (blue) for either 4 weeks (light color) or 12 weeks (dark color). The initial Fe-oxide-only and Fe-oxide-phosphate materials are shown in black for comparison. Iron transformation during incubation is primarily observed as decreasing amplitude of the two scattering peaks at ~ 7.6 and ~ 8.7 Å

dithionite-soluble Fe with mineralogy and in response to contrasting redox conditions (Fig. 5a). Namely, across all phosphate-addition treatments, dithionite-soluble P losses were greater in the lowland (− 43 ± 11%; n = 6) than the upland (− 24 ± 8%; n = 6) (p = 0.046), and Fh (− 11 ± 3%; n = 4) retained more phosphate than Gt or Hm (− 45 ± 7%; n = 8) (p < 0.001). In the lowland, Gt and Hm lost high amounts of dithionite-soluble P (− 60 ± 11% and − 58 ± 5%, respectively), consistent with high losses of dithionite-soluble Fe. In comparison, Fh, which gained small amounts of dithionite-soluble Fe, lost only 11 ± 3% of its dithionite-soluble P. In the upland, dithionite-soluble P decreased slightly for Fh (− 9.7 ± 6.9%) but more for Gt (− 38 ± 11%) and Hm (− 23 ± < 1%). The quartz treatments gained small amounts of dithionite-soluble P in both the lowland and upland (0.15 ± 0.05 µmol P g^{-1}) (Table 2).

The Fe-oxide-only (no phosphate) treatments started with very low dithionite-soluble P concentrations (< 1 µmol g^{-1}) that increased by an average 56 ± 15% in the lowlands and 21 ± 15% in the uplands (Fig. 5b), although the difference between landscape positions was not significant. Fh-only gained more P (+ 67 ± 29%) than Gt- and Hm-only treatments (+ 24 ± 43%), but this difference was only marginally significant (p = 0.07). The Qtz-only treatments lost small amounts of dithionite-soluble P over time (− 0.28 ± 0.21 µmol P g^{-1}; − 28 ± 21%) (Table 2).

Water-soluble P followed the same general trend as dithionite-soluble P but was 10–100 × lower in concentration (Table 2), indicating that P remained largely bound to the Fe oxides. For Fe-oxide-phosphate treatments, Fh retained the most water-soluble P over time, while water-soluble P in Gt-phosphate, Hm-phosphate, and quartz-phosphate all decreased (Table 2). In the Qtz-phosphate treatment, initial water-soluble P (0.50 ± 0.02 µmol P g^{-1}) was higher than dithionite-soluble P (0.40 ± 0.02 µmol P g^{-1}); however, after 12 weeks, dithionite-soluble P was about 6× higher than water-soluble P. Water-soluble P was initially below detection (< 0.01 µmol P g^{-1}) in Fe-oxide-only and quartz-only treatments and either stayed below detection limit or slightly increased over time (Table 2).

Changes in Fe-associated phosphate during incubation under contrasting redox conditions

P:Fe ratios, calculated from dithionite-soluble P and Fe, can further indicate changes in P (µmol) relative to Fe (mmol) over time (Table S5). For the Fe-phosphate treatments, P:Fe ratios decreased by − 14 ± 5% from the initial material but did not

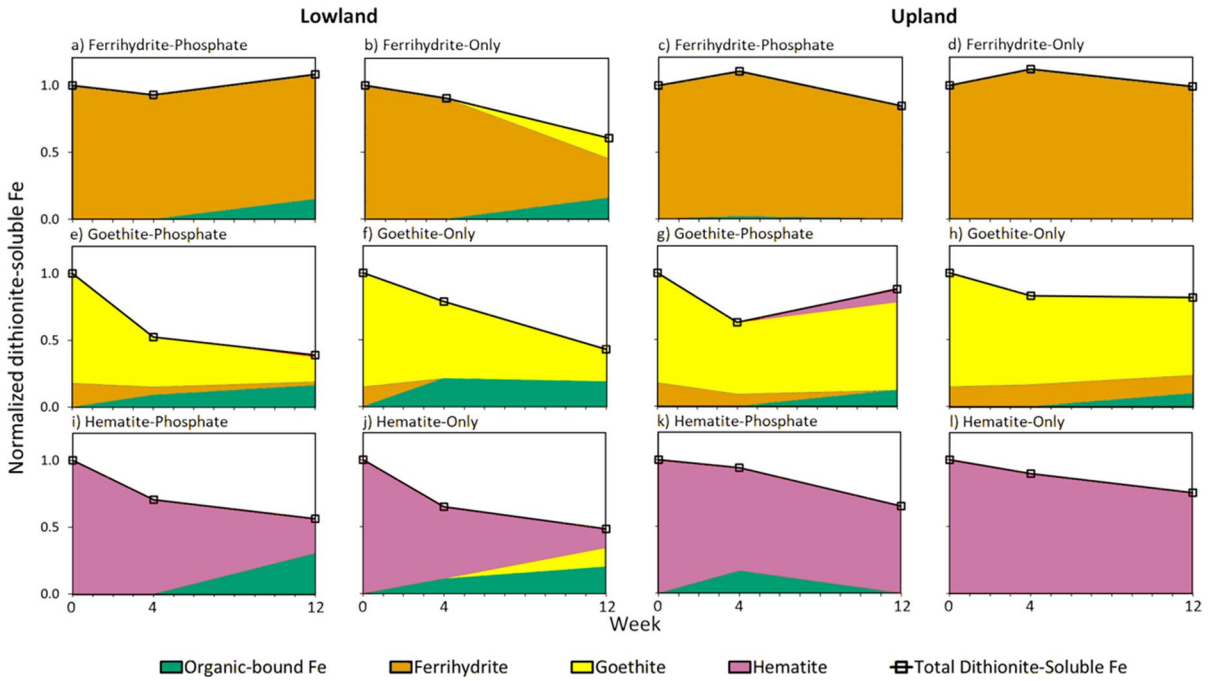

Fig. 4 Changes in total dithionite-soluble Fe (open square symbols) and Fe speciation (colored areas) over time normalized to initial measured values. Left two columns include lowland incubations (**a**, **b**, **e**, **f**, **i**, **j**) while the right two columns include upland incubations (**c**, **d**, **g**, **h**, **k**, **l**). Top row represents ferrihydrite incubations (**a–d**), middle row represents goethite incubations (**e–h**), and bottom row represents hematite incubation (**i–l**). Propagated analytical error is < 2%

change significantly from 4 to 12 weeks or with landscape position or mineralogy (Fig. S11). This result indicates that P loss generally tracked Fe loss for each treatment over time. However, excluding the organic-bound Fe to normalize P to the mass of Fe contained in Fe oxides (μmol P (mmol oxide-Fe)$^{-1}$), we found that Fe oxides retained or even gained P in all Fe-oxide-phosphate treatments. Specifically, P:Fe-oxide ratios initially decreased by $-11 \pm 7\%$ relative to the initial material by week 4 but then increased by $16 \pm 7\%$ by week 12. With this calculation, we assume that dithionite-soluble P equates to phosphate that is associated with Fe-oxides. We cannot exclude the possibility that this pool includes phosphate that has formed ternary complexes with organic-bound Fe(III) (e.g., Gerke and Hermann 1992), although the formation of these ternary complexes is uncertain (Sundman et al. 2016).

Iron-oxide-only treatments showed large increases in P:Fe over time (Fig. S11), consistent with increases in dithionite-soluble P despite Fe losses. Specifically, P:Fe ratios increased more for Fe-oxides incubated in the lowland relative to the upland ($p < 0.001$) and from 4 to 12 weeks ($p < 0.001$). All Fe-oxide minerals exhibited similar increases in P:Fe.

Discussion

In this study, we examined Fe-oxide dissolution and Fe transformation under natural contrasting soil redox regimes and its implications for phosphate sorption dynamics. We propose that Fe was mobilized from the Fe oxides into solution when soils underlying the vernal pond were saturated and reducing during early summer. Iron then reprecipitated as organic-bound Fe(III) and potentially also poorly crystalline Fe-oxides as the vernal pond dried and its soils drained and oxidized. In comparison, Fe-oxides underwent little to no transformation in the oxic and unsaturated upland soil. Contrary to expectations, Gt and Hm lost more Fe during the incubation than Fh, which we attribute to loss of colloidal Fe for Gt and Hm while Fe loss from Fh was driven by reductive dissolution. Phosphate

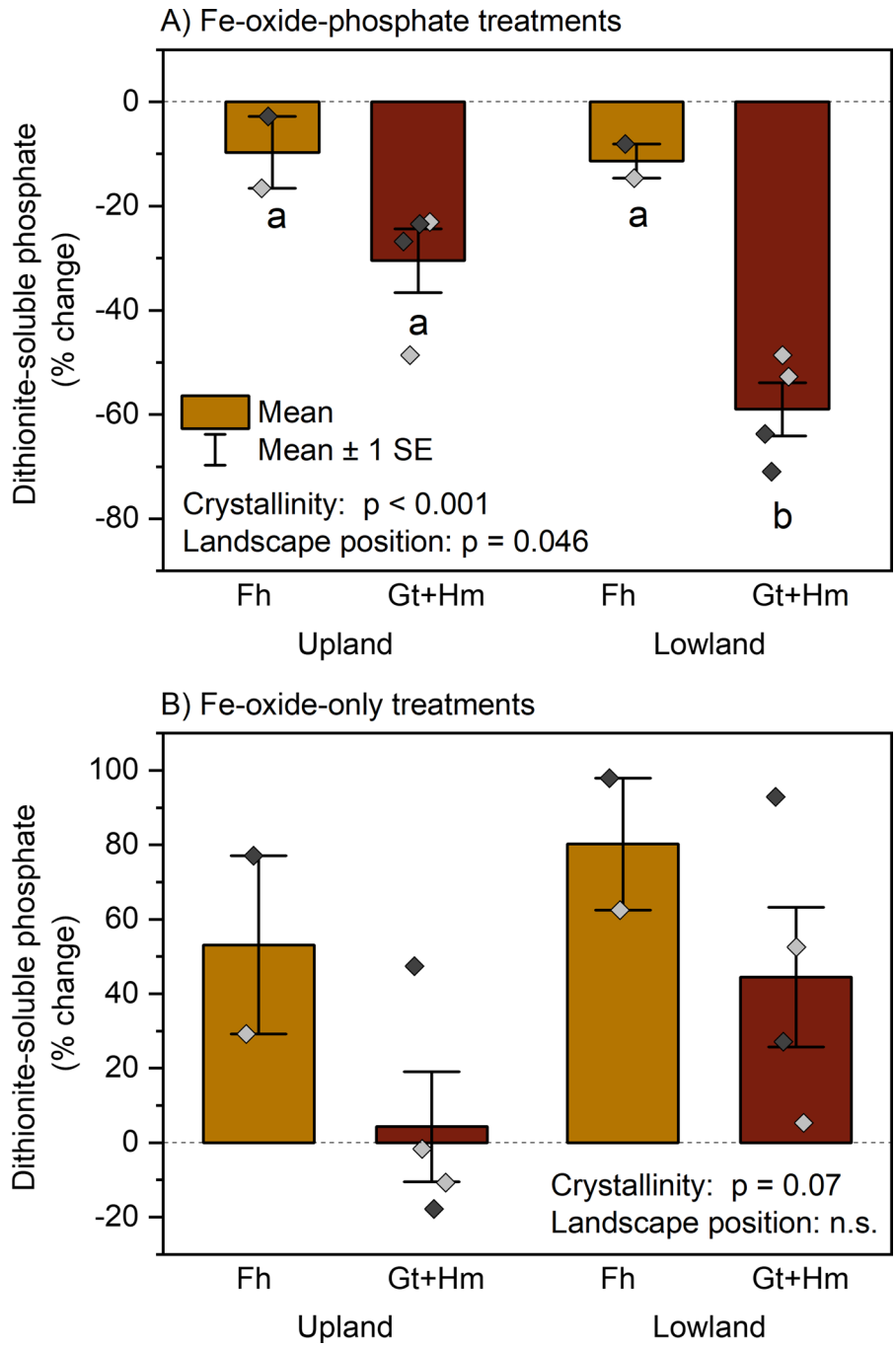

Fig. 5 Changes (%) in dithionite-soluble phosphate in incubated material relative to the initial pre-incubation material for **A** Fe-oxide-phosphate and **B** Fe-oxide-only treatments. Each bar represents the mean (±standard error) across incubation time (4 and 12 weeks) for each crystallinity (Fh or Gt + Hm) and landscape position (upland or lowland) combination within each phosphate treatment. Symbols indicate individual samples and are light grey for the 4 week incubation and dark grey for the 12 week incubation. The effects of landscape position and crystallinity are denoted by p-values determined using two-way ANOVA. Different letters indicate significant differences between means associated with each crystallinity/landscape position combination, as determined using a post-hoc Tukey test to $\alpha = 0.05$

followed a similar trend to Fe: it was released as Fe-oxides dissolved or were dispersed, but Fe-oxides that persisted during incubation retained or even gained phosphate. Below, we discuss the trends supporting this conceptual framework (Fig. 6).

Vernal ponds experience heterogenous redox conditions

Upland soils remained predominantly oxidizing over the incubation period whereas lowland soils exhibited spatial and temporal heterogeneity

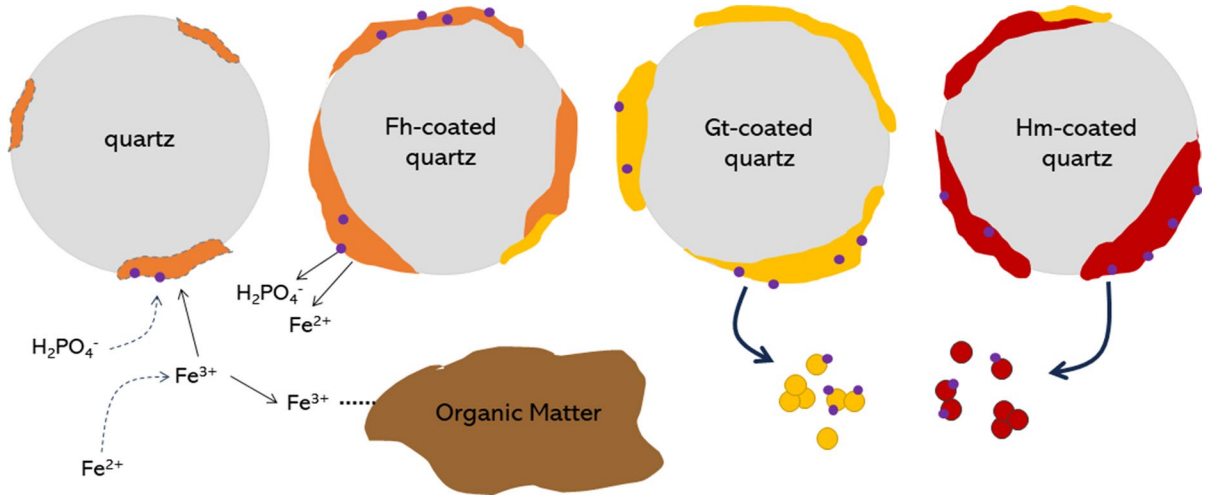

Fig. 6 Conceptual diagram of Fe and P mobilization from ferrihydrite (Fh, shown in orange), goethite (Gt, shown in yellow), and hematite (Hm, shown in red) coated quartz grains. Phosphate compounds adsorbed to Fe (oxyhydr)oxide surfaces are shown as purple circles. Fe and associated P losses from Gt and Hm were high and attributed to colloid detachment from the quartz surface and dispersal into solution. Relatively small losses of Fe and P from Fh were attributed to reductive dissolution of Fh and release of dissolved Fe^{2+} and phosphate ($H_2PO_4^{2-}$ at the pH conditions of the study) into solution. Dissolved Fe^{2+} in solution, sourced either from the synthetic Fe (oxyhydr)oxides or from the surrounding soil solution, was oxidized and associated with organic matter to form organic-bound Fe(III). Small quantities of phosphate in solution also sorbed onto existing or newly formed Fe (oxyhydr)oxides. Minor amounts of Gt formed in the phosphate-free Fh and Hm treatments, as indicated by the yellow patches

in redox as the pond dried. Specifically, the shallower portion of the pond shifted from reducing to oxidizing conditions over the study period while the deeper portion of the pond remained reducing (Barczok et al. 2023). The influence of shifting redox conditions could be observed in the vernal pond soils, which exhibited different properties with depth. Specifically, Fe and Mn oxides, present as coatings and/or discrete particles, were observed in both shallow and deep soils. These minerals form when dissolved Fe(II) and Mn(II) released into solution during reducing conditions reprecipitate as Fe(III) and Mn(III/IV)-oxides under oxidizing conditions. Indeed, pore water in vernal pond soils contained high concentrations of dissolved Fe (and P) during spring and early summer when the pond was flooded that decreased as the overlying surface water evaporated (Barczok et al. 2023). In organic-rich surface soils, Fe was diffusely associated with organo-mineral aggregates but also occurred as small particles within the aggregates. This Fe could represent organic-bound Fe(III) and/or small Fe oxide particles that associate with organic matter. Thus, the mixture of organic peat soil with Fe-oxide-coated minerals in our incubation experiment provides an appropriate comparison to the surrounding environment. In organic-poor soils at depth, Fe was present as coatings on the angular silicate grains that dominated soil composition.

It is important to note that Fe oxides incubated in the shallow and deep pond soils, which experienced contrasting redox regimes over 12 weeks, were composited prior to analysis. The observed trends discussed below therefore integrate processes across the deep side of the pond which maintained Fe reducing conditions and the shallow side of the pond which shifted to Fe oxidizing conditions, potentially leading to differences in the extents of Fe oxide dissolution and reprecipitation in each location. The contrast in redox regimes between the deep and shallow sides of the pond reflects environmental complexity and underscores the importance of studying Fe and P interaction in natural settings. Future studies would benefit from more spatially explicit characterization to evaluate how geochemical properties reflect redox heterogeneity.

Fe oxide loss and transformation differ between contrasting redox regimes

Prevailing reducing conditions in the lowland favored Fe oxide dissolution and Fe mobilization out of the mesh bags, leading to greater losses of Fe compared to the upland. Small Fe losses occurred in the upland despite constant oxidizing conditions and can be explained by ligand-promoted dissolution or by localized Fe reducing conditions due to rainfall or microbial activity that would not be captured by the bulk redox sensors (Liptzin and Silver 2009; Yang and Liptzin 2015).

Goethite and Hm lost more total Fe than Fh all incubations, which contradicts our hypothesis that Fe loss would be higher from Fh due to faster reductive dissolution. Rate constants for the complete reductive dissolution of ferrihydrite ($k' = 7.6–6.6 \times 10^{-4}$ s^{-1}) are two orders of magnitude higher than for goethite ($k' = 5.4 \times 10^{-6}$ s^{-1}) (Larsen and Postma 2000). We propose that Gt and Hm may have been preferentially lost as colloids from the mineral bags due to weaker interaction with the quartz. Although the pore size of the mesh bags (5 µm) was selected to retain the quartz sand (125 to 212 µm) and its Fe oxides coatings, it would not prevent movement of submicron-sized particles that detach from the quartz surface. All three Fe oxides used in this study commonly (Gt, Hm) or exclusively (Fh) occur as nanoparticles (Hochella et al. 2008), and the synthesis methods used here are reported to produce submicron-sized Gt and Hm crystals (Schwertmann and Cornell 2000). Although Fh could also be mobilized as colloids, previous studies note that Fh appears as masses of granular texture when coated on quartz sand while Gt and Hm appear either as discrete elongated particles (Gt) or spherical particles (Hm) (Rusch et al. 2010; Ilg et al. 2008; Guzman et al. 1994). These differences in morphology could indicate that Gt and Hm particles were more weakly adhered to the quartz surface and thus more susceptible to detachment and dispersion.

Indeed, more Fh was retained by the quartz sand during the mineral coating process than either Gt or Hm, indicating that Fh adhered more strongly. Similarly, Scheidegger et al. (1993) showed that Fh had 40% stronger affinity to quartz sand than Gt and 83% stronger affinity than Hm. Dispersion of Fe oxide colloids is also supported by higher Fe losses from Gt- and Hm-coated quartz during phosphate sorption than from Fh-coated quartz. Ilg et al. (2008) observed similar Fe loss during phosphate sorption onto Gt-coated sand and attributed it to repulsion from the quartz surface caused by changing surface charge of Gt as more phosphate adsorbed. However, it is important to note that phosphate sorption cannot explain Fe losses during incubation since similar losses were observed in phosphate and no phosphate treatments. Detachment and dispersion of Gt and Hm colloids during incubation may have resulted from interactions with acidic and low ionic strength water infiltrating through the soils (Ryan and Gschwend 1994). Loss of colloidal Fe may also be indicated by high concentrations of water-soluble Fe in the Hm and Gt treatments that were not present in the Fh treatments. High water-soluble Fe, which represents all Fe that is mobilized during water extraction and passes through a 0.45 µm filter, could consist of colloidal Fe (Aiken et al. 2011) that has detached from the quartz sand. While we cannot exclude the possibility that the water-soluble Fe is truly dissolved Fe, we did not observe an increase in water-soluble Fe in our Fh samples which would be indicative of reductive dissolution.

Iron transformation was more pronounced in the lowland than the upland, which we attribute to dissolution of Fe-oxides during reducing conditions and subsequent formation of organic-bound Fe(III) and smaller quantities of Fe oxides during oxidizing conditions. Indeed, organic-bound Fe(III) was present at an average 37% ± 9% in lowland treatments but only 4% ± 4% in upland treatments after 12 weeks. This observation is consistent with other studies showing preferred formation of organic-bound Fe(III) over Fe oxides under acidic conditions similar to those in our study (Karlsson and Persson 2010; Sundman et al. 2014).

Although Fe transformation in the lowland was dominated by conversion from Fe-oxides to organic-bound Fe(III), some mineral formation was observed. Specifically, Gt was formed in the Fh- and Hm-only treatments. Goethite can form from Fh via Ostwald ripening (Cornell and Schwertmann 2003; Hansel et al. 2005) or through Fe(II)-facilitated crystallization (Williams and Scherer 2004; Hansel et al. 2005; Pedersen et al. 2005). Goethite can also precipitate following reductive dissolution of ferrihydrite (Hansel et al. 2003). Although structural similarities often make it difficult to distinguish between synthetic ferrihydrite and goethite using EXAFS (O'Day et al.

2004), particularly at k < 10 Å, the Fe oxides used in this study exhibited clear spectral differences (Fig. 3). Specifically, spectral amplitudes between 7 to 9 Å increased from Fh to Gt to Hm. Sun et al. (2018) similarly observed that ferrihydrite could be differentiated from goethite phases due to differences in amplitudes in this region, although nano-goethite and ferrihydrite were relatively indistinguishable.

No Gt was formed in the Fe-oxide-phosphate treatments, indicating the potential for sorbed phosphate to inhibit mineral transformation (O'Loughlin et al. 2021; Borch et al. 2007; Gálvez et al. 1999). Previous studies have shown that the addition of phosphate to Fh hinders the formation of Gt, likely by hindering Fh dissolution rather than the nucleation and growth of Gt (Borch et al. 2007; Gálvez et al. 1999). Consistent with phosphate-inhibited dissolution, the Fh-phosphate treatments experienced negligible Fe loss and transformation (Fig. 4), although additional studies are needed to confirm this observation. We did not observe Fh formation in any treatments, although Fe dissolved from Fh could feasibly have reprecipitated as Fh or transformed into nano-Gt and led to no observable changes in mineralogy.

Effects of Fe-oxide loss and transformation on P retention

Phosphate loss from Fe-oxide-phosphate treatments followed trends for Fe loss, indicating that phosphate was released into solution as Fe-oxides dissolved or was bound to colloidal Fe that detached from the quartz grains. Similar to Fe, more phosphate was lost from Gt and Hm treatments than from Fh. Given that phosphate is primarily associated with Fe-oxides in the initial material, we would expect that phosphate losses are directly proportional Fe losses, i.e., P/Fe ratios do not change. Indeed, P/Fe ratios either did not change or decreased in the Fe-oxide-phosphate treatments (Fig. S11), indicating that P was released but some Fe was retained as organic-bound Fe(III) that did not bind P. However, P/oxide-Fe ratios initially decreased but then increased by week 12, from which we infer that phosphate was sorbed from solution. It is important to note that the Fh might not have been fully saturated with phosphate. Indeed, Borch et al. (2007) report phosphate adsorption on Fh at levels twice as high as in this study. It is therefore likely that phosphate-free Fh surfaces were preferentially dissolved and/or that any released phosphate was rapidly sequestered by the remaining Fh.

For all Fe-oxide-only treatments, increases in P:Fe-oxide ratios are similarly attributed to sorption of phosphate from soil solution onto the Fe-oxide surfaces. The larger increase in the lowland versus the upland can be explained by more phosphate being available in the flooded lowland compared to the dry upland (Barczok et al. 2023). In addition, precipitation of short range ordered Fe-oxide phases in the lowland during oxidizing conditions could potentially increase phosphate sorption capacity. The fact that there was no statistical difference between initial Fe-oxide mineralogy and the increase in P:Fe ratios indicates that all of the Fe-oxides had similar capacity to adsorb phosphate from solution over the timescales of this study. While we cannot discount the possibility that phosphate formed a ternary complex with organic-bound Fe(III) (Gerke and Hermann 1992), these complexes were not observed in experimental studies of Fe(III)-OM-phosphate systems (Sundman et al. 2016). As we measured phosphate as molybdate reactive P, a proxy for inorganic phosphate which does not include organic P, we do not expect our findings to be influenced by organic P.

Conclusion

In this study, we observe that Fe-oxides (ferrihydrite, goethite, hematite) experience distinct differences in Fe loss, Fe transformation, and consequent ability to adsorb phosphate when incubated under contrasting redox regimes. Iron oxide dissolution and Fe transformation reactions in vernal pond soils, a redox-dynamic regime, were driven by reducing conditions that shifted to oxidizing conditions over the season. We confirm our first hypothesis that Fe oxides incubated in lowland soils lost more Fe and P and also experienced more transformation, primarily via formation of organic-bound Fe(III), compared to upland treatments. In contrast to our expectations that crystalline oxides would experience less dissolution and leaching, goethite and hematite lost more Fe and P than ferrihydrite. We attribute this result to detachment and loss of colloidal Fe and associated P from the goethite and hematite. We also confirm our third hypothesis that Fe phases with a higher capacity for phosphate uptake would form in the lowlands,

presumably during oxidizing conditions that promote precipitation of short range ordered Fe oxide phases. However, P retention by these phases was small relative to P loss, and formation of organic-bound Fe(III) under acidic conditions likely limited reprecipitation of Fe oxides and their associated capacity for phosphate sorption. Overall, we conclude that both reductive dissolution and colloid dispersion resulted in the loss of phosphate associated with Fe oxides out of the mineral bags.

These results reinforce the importance of understanding Fe dynamics in order to predict P bioavailability under changing hydrology and redox conditions. Phosphorus sorption to minerals and Fe–P-redox interactions have been identified as key processes that need to be included in Earth System Models to improve climate-carbon cycling models (Reed et al. 2015). Yet, we don't have a complete understanding of how hydrologic and redox changes in soils regulate Fe speciation and P bioavailability to plants and microorganisms. We demonstrate here that reducing conditions result in loss of P from Fe oxides, but that the magnitude of the loss varies based on the Fe oxide mineralogy. Additionally, we demonstrate that, while SRO Fe oxides are typically assumed to be the most important phases for regulating P mobilization, crystalline Fe-oxide phases such as goethite and hematite can play an equal or greater role.

Acknowledgements We would like to thank Shannon Joseph for field and lab work assistance, as well as Lindsey Yazbek, Raihan Chowdhury, and Mallory Klein for help with mesh bag assembly.

Author contributions MB developed methodologies, conducted the experiments, performed data analyses, and wrote the manuscript. CS and ND contributed to conceptualization, methodology, and experimentation. LKC contributed to conceptualization, funding acquisition, and review and editing of the manuscript. DS contributed to project supervision and review and editing of the manuscript. EH provided funding, supervised the project, and contributed to conceptualization, methodology, and writing.

Funding This work was supported by grants from the National Science Foundation (EAR-1609027 and OPP-2006194) and the Kent State Environmental Science and Design Research Initiative to Herndon and Kinsman-Costello. Portions of this work were performed at GeoSoilEnviroCARS (Sector 13) and 12-BMB (Sector 12), Advanced Photon Source (APS), Argonne National Laboratory. GeoSoilEnviroCARS is supported by the National Science Foundation – Earth Sciences (EAR-1128799) and Department of Energy – GeoSciences (DE-FG02-94ER14466). Use of the Advanced Photon Source was supported by the U. S. Department of Energy, Office of Science, Office of Basic Energy Sciences, under Contract No. DE-AC02-06CH11357.

Data availability All datasets used in this manuscript are provided in tables in the main text or supporting information.

Declarations

Competing interests The authors declare no financial or non-financial conflicts of interest.

References

Aiken GR, Hsu-Kim H, Ryan JN (2011) Influence of dissolved organic matter on the environmental fate of metals, nanoparticles, and colloids. Environ Sci Technol 45(8):3196–3201

Ajmal Z, Muhmood A, Usman M, Kizito S, Lu J, Dong R, Wu S (2018) Phosphate removal from aqueous solution using iron oxides: Adsorption, desorption and regeneration characteristics. J Colloid Interf Sci 528:145–155

Bache BW, Williams EG (1971) A phosphate sorption index for soils. J Soil Sci 22:289–301

Balint R, Said-Pullicino D, Ajmone-Marsan F (2015) Copper dynamics under alternating redox conditions is influenced by soil properties and contamination source. J Contam Hydrol 173:83–91

Barczok M, Smith C, Di Domenico N, Kinsman-Costello L, Herndon E (2023) Variability in soil redox response to seasonal flooding in a vernal pond. Front Environ Sci Biogeochem Dyn. https://doi.org/10.3389/fenvs.2023.1114814

Bhattacharyya A, Schmidt MP, Stavitski E, Martínez CE (2018) Iron speciation in peats: chemical and spectroscopic evidence for the co-occurrence of ferric and ferrous iron in organic complexes and mineral precipitates. Org Geochem 115:124–137

Blackwood CB, Smemo KA, Kershner MW, Feinstein LM, Valverde-Barrantes OJ (2013) Dexay of ecosystem differences and decoupling of tree community-soil environment relationships at ecotones. Ecol Monogr 83(3):403–417

Borch T, Masue Y, Kukkadapu RK, Fendorf S (2007) Phosphate imposed limitations on biological reduction and alteration of ferrihydrite. Environ Sci Technol 41:166–172

Brooks SC, Taylor DL, Jardine PM (1996) Reactive transport of EDTA-complexed cobalt in the presence of ferrihydrite. Geochim Cosmochim Acta 60:1899–1908

Bryce C, Blackwell N, Schmidt C, Otte J, Huang Y, Kleindienst S, Tomaszewski E, Schad M, Warter V, Peng C, Byrne JM, Kappler A (2018) Microbial anaerobic Fe(II) oxidation—ecology, mechanisms and environmental implications. Environ Microbiol 20(10):3462–3483

Caraco N, Cole J, Likens GE (1990) A comparison of phosphate immobilization in sediments of freshwater and coastal marine systems. Biogeochemistry 9:277–290

Chacón N, Silver WL, Dubinsky EA, Cusack DF (2006) Iron reduction and soil phosphorus solubilization in humid

tropical forests soils: the roles of labile carbon pools and an electron shuttle compound. Biogeochemistry 78:67–84

Chapin FS, Matson PA, Mooney HA, Vitousek PM (2002) Principles of terrestrial ecosystem ecology. Springer, New York

Chen C, Thompson A (2018) Ferrous iron oxidation under varying pO_2 levels: the effect of Fe(III)/Al(III) oxide minerals and organic matter. Environ Sci Technol 52:597–606

Colombo C, Palumbo G, He J-Z, Pinton R, Cesco S (2014) Review on iron availability in soil: interaction of Fe minerals, plants, and microbes. J Soil Sediment 14(3):538–548

Cornell RM, Schwertmann U (2003) The iron oxides: structure, properties, reactions, occurrences and uses. Wiley, Weinheim

Coward EK, Thompson AT, Plante AF (2017) Iron-mediated mineralogical control of organic matter accumulation in tropical soils. Geoderma 306:206–216

Essington ME (2015) Soil and water chemistry: an integrative approach. CRC Press, Boca Raton

Gálvez N, Barrón V, Torrent J (1999) Effect of phosphate on the crystallization of hematite, goethite, and lepidocrocite from ferrihydrite. Clay Clay Miner 47(3):304–311

Giannetta B, Plaza C, Siebecker MG, Aquilanti G, Vischetti C, Plaisier JR, Juanco M, Sparks DL, Zaccone C (2020) Iron speciation in organic matter fractions isolated from soils amended with biochar and organic fertilizers. Environ Sci Technol 54:5093–5101

Gerke J, Hermann R (1992) Adsorption of orthophosphate to humic–Fe-complexes and to amorphous Fe-oxide. Zeitschrift Für Pflanzenernährung Und Bodenkunde 155(3):233–236

Gu C, Dam T, Hart SC, Turner BL, Chadwick OA, Berhe AA, Hu Y, Zhu M (2020) Quantifying uncertainties in sequential chemical extraction of soil phosphorus using XANES spectroscopy. Environ Sci Technol 54:2257–2267

Guzman G, Alcantara E, Barron V, Torrent J (1994) Phytoavailability of phosphate adsorbed on ferrihydrite, hematite, and goethite. Plant Soil 159:219–225

Handler RM, Frierdich AJ, Johnson CM, Rosso KM, Beard BL, Wang C, Latta DE, Neumann A, Pasakarnis T, Premaratne WAPJ, Scherer MM (2014) Fe(II)-catalyzed recrystallization of goethite revisited. Environ Sci Technol 48:11302–11311

Hansel CM, Benner SG, Neiss J, Dohnalkova A, Kukkadapu RK, Fendorf S (2003) Secondary mineralization pathways induced by dissimilatory iron reduction of ferrihydrite under advective flow. Geochim Cosmochim Acta 67:2977–2992

Hansel CM, Benner SG, Fendorf S (2005) Competing Fe(II)-induced mineralization pathways of ferrihydrite. Environ Sci Technol 39:7147–7153

Herndon E, AlBashaireh A, Singer D, Chowdhury TR, Gu B, Graham D (2017) Influence of iron redox cycling on organo-mineral associations in arctic tundra soil. Geochim Cosmochim Acta 207:210–231

Herndon EM, Kinsman-Costello L, Duroe KA, Mills J, Kane ES, Sebestyen SD, Thompson AA, Wullschleger SD (2019) Iron (oxyhydr)oxides serve as phosphate traps in tundra and boreal peat soils. J Geophys Res Biogeogr 124:227–246

Hochella M, Lower SK, Maurice PA, Penn RL, Sahai N, Sparks DL, Twining BS (2008) Nanominerals, mineral nanoparticles, and earth systems. Science 319:1631–1635

Ilg K, Dominik P, Kaupenjohann M, Siemens J (2008) Phosphorus-induced mobilization of colloids: model systems and soils. Eur J Soil Sci 59:233–246

Kappler A, Bryce C, Mansor M, Lueder U, Byrne JM, Swanner ED (2021) An evolving view on biogeochemical cycling of iron. Nat Rev Microbiol 19:360–374

Karlsson T, Persson P (2010) Coordination chemistry and hydrolysis of Fe(III) in a peat humic acid studied by X-ray absorption spectroscopy. Geochim Cosmochim Acta 74:30–40

Khare N, Hesterberg D, Martin JD (2005) XANES investigation of phosphate sorption in single and binary systems of iron and aluminum oxide minerals. Environ Sci Technol 39:2152–2160

Kiczka M, Wiederhold JG, Frommer J, Voegelin A, Kraemer SM, Bourdon B, Kretzschmar R (2011) Iron speciation and isotope fractionation during silicate weathering and soil formation in an alpine glacier forefield chronosequence. Geochim Cosmochim Acta 75:5559–5573

Kögel-Knabner I, Amelung W, Cao Z, Fiedler S, Frenzel P, Jahn R, Kalbitz K, Kölbl A, Schloter M (2010) Biogeochemistry of paddy soils. Geoderma 157:1–14

Lalonde K, Mucci A, Ouellet A, Gélinas Y (2012) Preservation of organic matter in sediments promoted by iron. Nature 483(7388):198–200

Lambers H, Chapin FS, Pons TL (2008) Plant physiological ecology, vol 2. Springer, New York, pp 11–99

Larsen O, Postma D (2000) Kinetics of reductive bulk dissolution of lepidocrocite, ferrihydrite, and goethite. Geochim Cosmochim Acta 65:1367–1379

Lin Y, Bhattacharyya A, Campbell AN, Nico PS, Pett-Ridge J, Silver WL (2018) Phosphorus fractionation responds to dynamic redox conditions in a humid tropical forest soil. J Geophys Res Biogeogr 123:3016–3027

Liptzin D, Silver WL (2009) Effects of carbon additions on iron reduction and phosphorus availability in a humid tropical soil. Soil Biol Biochem 41:1696–1702

Mallet M, Barthélémy K, Ruby C, Renard A, Naille S (2013) Investigation of phosphate adsorption onto ferrihydrite by X-ray photoelectron spectroscopy. J Colloid Interfaces Sci 407:95–101

Mikutta C, Mikutta R, Bonneville S, Wagner F, Voegelin A, Christl I, Kretzschmar R (2008) Synthetic coprecipitates of exopolysaccharides and ferrihydrite, Part I: characterization. Geochim Cosmochim Acta 72:1111–1127

Moormann FR, van Breemen N (1978) Rice: soil, water, land. International Rice Research Institute, Los Baños

Mortimer CH (1941) The exchange of dissolved substances between mud and water in lakes. J Ecol 29(2):280–329

National Oceanic Atmospheric Agency/National Centers for Environmental Information (2021) Climate data Online. Subset used 1998–2018. Accessed 27 July 2021

Newville M (2013) Larch: an analysis package for XAFS and related spectroscopies. J Phys Conf Ser 430:012007

Newville M, Boyanov BI, Sayers DE (1999) Estimation of uncertainties in XAFS data. J Synchrotron Rad 6:264–265

O'Day PA, Rivera N Jr, Root R, Carroll SA (2004) X-ray absorption spectroscopic study of Fe reference compounds

for the analysis of natural sediments. Am Mineral 89(4):572–585
O'Loughlin EJ, Boyanov MI, Gorski CA, Scherer MM, Kemner KM (2021) Effects of Fe(III) oxide mineralogy and phosphate on Fe(II) secondary mineral formation during microbial iron reduction. Minerals 11:149
Paludan C, Jensen HS (1995) Sequential extraction of phosphorus in freshwater wetland and lake sediment: Significance of humic acids. Wetlands 4:365–373
Patrick WH Jr, DeLaune RD (1977) Chemical and biological redox systems affecting nutrient availability in the coastal wetlands. Geosci Man 18(13):137
Pedersen HD, Postma D, Jakobsen R, Larsen O (2005) Fast transformation of iron oxyhydroxides by the catalytic action of aqueous Fe(II). Geochim Cosmochim Acta 69:3967–3977
Ravel B, Newville M (2005) ATHENA, ARTEMIS, HEPHAESTUS: data analysis for X-ray absorption spectroscopy using IFEFFIT. J Synchrotron Radiat 12(4):537–541
Reed SC, Yang X, Thornton PE (2015) Incorporating phosphorus cycling into global modeling efforts: a worthwhile, tractable endeavor. New Phytol 208:324–329
Roden EE, Edmonds J (1997) Phosphate mobilization in iron-rich anaerobic sediments: microbial Fe(III) oxide reduction versus iron-sulfide formation. Arch Hydrobiol 139(3):347–378
Rusch B, Hanna K, Humbert B (2010) Coating of quartz silica with iron oxides: characterization and surface reactivity of iron coating phases. Colloid Surface A 353:172–180
Ruttenberg KC, Sulak DJ (2011) Sorption and desorption of dissolved organic phosphorus onto iron (oxyhydr)oxides in seawater. Geochim Cosmochim Acta 75:4095–4112
Ryan JN, Gschwend PM (1994) Effect of solution chemistry on clay colloid release from an iron oxide-coated aquifer sand. Environ Sci Technol 28:1717–1726
Schaefer MV, Gorski CA, Scherer MM (2011) Spectroscopic evidence for interfacial Fe(II)–Fe(III) electron transfer in clay mineral. Environ Sci Technol 45:540–545
Scheidegger A, Borkovec M, Sticher H (1993) Coating of silica sand with goethite: preparation and analytical identification. Geoderma 58:43–65
Schwertmann U, Cornell RM (2000) Iron oxides in the laboratory: preparation and characterization, 2nd completely rev. and extended edn. Wiley-VCH, Weinheim
Sun J, Mailloux BJ, Chillrud SN, van Geen A, Thompson A, Bostick BC (2018) Simultaneously quantifying ferrihydrite and goethite in natural sediments using the method of standard additions with X-ray absorption spectroscopy. Chem Geol 476:248–259
Sjöstedt C, Persson I, Hesterberg D, Kleja DB, Borg H, Gustafsson JP (2013) Iron speciation in soft-water lakes and soils as determined by EXAFS spectroscopy and geochemical modelling. Geochim Cosmochim Acta 105:172–186
Slomp CP, Van der Gaast SJ, Van Raaphorst W (1996) Phosphorus binding by poorly crystalline iron oxides in North Sea sediments. Mar Chem 52(1):55–73
Sundman A, Karlsson T, Laudon H, Persson P (2014) XAS study of iron speciation in soils and waters from a boreal catchment. Chem Geol 364:93–102
Sundman A, Karlsson T, Sjöberg S, Persson P (2016) Impact of iron-organic matter complexes on aqueous phosphate concentrations. Chem Geol 426:109–117
Tessier A, Rapin F, Carignan R (1985) Trace metals in oxic lake sediments: possible adsorption onto iron oxyhydroxides. Geochim Cosmochim Acta 49(1):183–194
Thamdrup B (2000) Bacterial manganese and iron reduction in aquatic sediments. Adv Microb Ecol 16:41–84
Thompson A, Chadwick OA, Rancourt DG, Chorover J (2006) Iron-oxide crystallinity increases during soil redox oscillations. Geochim Cosmochim Acta 70(7):1710–1727
Thompson A, Rancourt DG, Chadwick OA, Chorover J (2011) Iron solid-phase differentiation along a redox gradient in basaltic soils. Geochim Cosmochim Acta 75:119–133
Tomaszewski EJ, Cronk SS, Gorski CA, Ginder-Vogel M (2016) The role of dissolved Fe(II) concentration in the mineralogical evolution of Fe (hydr)oxides during redox cycling. Chem Geol 438:163–170
USGCRP (2018) Impacts, risks, and adaptation in the United States. In: Reidmiller DR, Avery CW, Easterling DR, Kunkel KE, Lewis KLM, Maycock TK, Stewart BC (eds) Fourth National Climate Assessment, vol II. Global Change Research Program, Washington. https://doi.org/10.7930/NCA4.2018
Vitousek PM, Porder S, Houlton BZ, Chadwick OA (2010) Terrestrial phosphorus limitation: mechanisms, implications, and nitrogen–phosphorus interactions. Ecol Appl 20(1):5–15
Vogelsang V, Fiedler S, Jahn R, Kaiser K (2016) In-situ transformation of iron-bearing minerals in marshland-derived paddy subsoil. Eur J Soil Sci 67:676–685
Wang Y, Shen Z, Niu J, Liu R (2009) Adsorption of phosphorus on sediments from the Three-Gorges Reservoir (China) and the relation with sediment compositions. J Hazard Mater 162:92–98
Weber KA, Achenbach LA, Coates JD (2006) Microorganisms pumping iron: anaerobic microbial iron oxidation and reduction. Nat Rev Microbiol 4:752–764
Westheimer FH (1987) Why nature chose phosphates. Science 235(4793):1173–1178
Williams AGB, Scherer MM (2004) Spectroscopic evidence for Fe(II)–Fe(III) electron transfer at the iron oxide–water interface. Environ Sci Technol 38:4782–4790
Winkler P, Kaiser K, Thompson A, Kalbitz K, Fiedler S, Jahn R (2018) Contrasting evolution of iron phase composition in soils exposed to redox fluctuations. Geochim Cosmochim Acta 235:89–102
Yang H, Liptzin D (2015) High potential for iron reduction in upland soils. Ecology 96:2015–2020